

Partial Volume Effect (PVE) Correction in Single Photon Emission Computed Tomography (SPECT) Imaging

Koffi N'guessan Placide Gabin Allangba^{1, 2, 3, 5, 6, *}, Annick Kouame Koutouan², Alessia Giuliano⁶, Zié Traoré^{4, 5}, Antonio Traino⁶

¹Laboratory of Environmental Science and Technology, University Jean Lorougnon Guédé, Daloa, Côte d'Ivoire

²Laboratory of Biophysics and Nuclear Medicine (LBNM), University Félix Houphouët-Boigny, Abidjan, Côte d'Ivoire

³Laboratory of Fundamental and Applied Physics (LFAP), University Nangui Abrogoua, Abidjan, Côte d'Ivoire

⁴Nuclear Physics and Radiation Protection Team, Laboratory of Material Sciences Environment and Solar Energy, University Félix Houphouët-Boigny, Abidjan, Côte d'Ivoire

⁵Department of Medical Physics, University of Trieste and International Centre for Theoretical Physics (ICTP), Trieste, Italy

⁶Unit of Medical Physics, Pisa University Hospital "Azienda Ospedaliero-Universitaria Pisana", Pisa, Italy

Email address:

pgallangba@gmail.com (Koffi N'guessan Placide Gabin Allangba)

*Corresponding author

To cite this article:

Koffi N'guessan Placide Gabin Allangba, Annick Kouame Koutouan, Alessia Giuliano, Zié Traoré, Antonio Traino. Partial Volume Effect (PVE) Correction in Single Photon Emission Computed Tomography (SPECT) Imaging. *Radiation Science and Technology*. Vol. 9, No. 3, 2023, pp. 26-35. doi: 10.11648/j.rst.20230903.11

Received: August 5, 2023; **Accepted:** August 23, 2023; **Published:** September 6, 2023

Abstract: Quantitative analyses in Nuclear Medicine are essential, hence growing interest in algorithms that make nuclear medical data more reliable and accurate. The Partial Volume Effect (PVE) is the most important factor of loss of quantification in Nuclear Medicine, particularly for evaluation in regions of interest (ROIs) smaller than the Full Width at Half Maximum (FWHM) of the Point Spread Function (PSF) of the imaging system. This study is focused on applying a post-reconstruction correction algorithm of PVE at regional level in SPECT imaging. After a quantitative evaluation of the sigma of the PSF of the SPECT imaging system, several experimental situations have been studied using the standard IEC NEMA Body phantom, which contains six spherical inserts that mimic lesions with diameters of 10 mm, 13 mm, 17 mm, 22 mm, 28 mm, and 37 mm. They were filled with ^{99m}Tc mixed with distilled water using a sphere-to-background activity concentration ratio of 10: 1. The experimental measurements were carried out with two activity concentrations of ^{99m}Tc: 170.2 KBq/mL and 451.0 KBq/mL. The PVE correction approach has been employed in this paper to correct PVE on spherical volumes of interest (VOIs) of different sizes and to evaluate the recovery of quantitative data. Images were reconstructed using Ordered-Subset Expectation Maximization (OSEM) algorithm, applying scatter and attenuation corrections of photons, both with and without the application of the Butterworth filter. In the end, a post-reconstruction algorithm implemented with MATLAB was used. The mean difference rate between the corrected image and the raw image of the medium-sized spheres (13mm, 17mm, and 22mm) gives an improvement rate of about 70% of the PVE correction for unfiltered images at 170.2 KBq/mL. This work showed that the application of the PVE correction method recovers lost activity concentration with accuracy.

Keywords: Partial Volume Effect, Recovery, Point Spread Function, Post-Reconstruction Correction Algorithm, SPECT Imaging

1. Introduction

In nuclear medicine, gamma cameras and SPECT/CT (CT: Computed Tomography) systems are routinely used for

quantitative imaging. Regarding the technical aspect of the image generation process, the partial volume effect (PVE) is one of the most common factors that affect the imaging of objects. Moreover, the activity quantification is underestimated for objects smaller than 2.5 times the Full

width Half Maximum (FWHM) of the point spread function (PSF) of the imaging system used when their activity is higher than that in the surrounding regions [1-3].

The measured uptake is obtained when the object uptake is convoluted with the system PSF. Therefore, PVE depends on the imaging system's spatial resolution. In general, PVE is seen as the moving counts between different image regions. The PVE not only affects visual SPECT and PET (Positron Emission Tomography) images evaluation but also the determination of radionuclide uptake in absolute units as necessary, for example for dosimetry of radionuclide therapy. However, the PVE is composed of two effects: spill-out and spill-in, which make sense when focusing on a volume of interest (VOI) in which the activity needs to be quantified. Indeed, there is a spill-out when the activity is underestimated in a region that has higher activity than its surroundings and there is a spill-in when the activity is overestimated in a region that has lower activity than its surroundings. Overall, PVE introduces quantitative biases [4]. Several methods have been developed and applied in different works to correct PVE [5-10].

The algorithm implemented in MATLAB using the deconvolution method in post-reconstruction to correct images was developed by Di Martino et al and applied to PET images [5]. This method was used to correct the PVE at the regional level to improve image quality and quantification of activity accurately. In this work, this algorithm is applied for the first time to SPECT images.

2. Materials and Methods

2.1. Materials and Imaging Protocol

In this work, a SPECT/CT machine, model Discovery NM/CT 670 (General Electric Company, Boston, MA, USA), was employed for image acquisition. Firstly, the PSF was experimentally evaluated using a point source of ^{99m}Tc . Secondly, the images of a standard IEC NEMA Body

phantom, filled with ^{99m}Tc mixed with distilled water, were acquired to test the PVE correction algorithm. This phantom contains six sphere inserts with inner diameters of 10 mm (520 mm^3), 13 mm (1150 mm^3), 17 mm (2570 mm^3), 22 mm (5570 mm^3), 28 mm (11490 mm^3), and 37 mm (26510 mm^3), representing various lesion sizes. The ^{99m}Tc isotope activities used were measured using a dose calibrator (Atomlab 500 Dose Calibrator, Biodex, New York, NY, USA). The clinical protocol Transarterial Radioembolization (TARE) was used. The images were acquired in tomographic mode using a matrix size of 128×128 , Low Energy High Resolution (LEHR) collimator, energy window of 20%, and center at 140 keV. The SPECT images were reconstructed using Ordered-Subset Expectation Maximization (OSEM) algorithm with 2 iterations, 10 subsets, both with and without the Butterworth filter (cut-off frequency (fc) 0.48 and power (p) 10). CT Attenuation Correction and Scatter Correction (ACSC) of photons were applied. The PVE correction algorithm was implemented in MATLAB (The MathWorks, Inc., Natick, MA, USA) and all the images (raw and corrected) were analyzed using MATLAB (The MathWorks, Inc., Natick, MA, USA), LIFEx [11], ImageJ [12] and Xeleris software (General Electric Company, Boston, MA, USA).

2.2. Methods

2.2.1. Theoretical Focus

The post-reconstruction analytical method is explained in detail in the paper of Di Martino et al. [5]. In this part, some key formulas have been summarized. This method is based on the exact analytical deconvolution of the PSF of the imaging system at the regional level. The application uses a basic assumption where a single source with homogeneous activity is surrounded by a homogeneous background. The PSF of a 3D SPECT imaging system can be modeled as equation 1.

$$PSF_{3D}(x, \sigma_x; y, \sigma_y; z, \sigma_z) = \frac{1}{(\sigma_x, \sigma_y, \sigma_z)\sqrt{8\pi^3}} e^{-\frac{x^2}{\sigma_x^2} - \frac{y^2}{\sigma_y^2} - \frac{z^2}{\sigma_z^2}} = PSF_{1D}(x, \sigma_x) \times PSF_{1D}(y, \sigma_y) \times PSF_{1D}(z, \sigma_z) \quad (1)$$

In this method, 3D source can be described by equation 2, where “s” is the source counts concentration, “b” the background counts concentration, and “l” the source dimension.

$$S_{3D}(x, l_x; y, l_y; z, l_z) = \begin{cases} s \forall (x, y, z) \in \left[-\frac{l_x}{2}; \frac{l_x}{2}\right]; \left[-\frac{l_y}{2}; \frac{l_y}{2}\right]; \left[-\frac{l_z}{2}; \frac{l_z}{2}\right] \\ b \text{ outside} \end{cases} \quad (2)$$

Linearity properties of the convolution operator give equation 3,

$$L_{3D}(x, l_x, \sigma_x; y, l_y, \sigma_y; z, l_z, \sigma_z) = S_{3D}(x, l_x; y, l_y; z, l_z) \times PSF_{3D}(x, \sigma_x; y, \sigma_y; z, \sigma_z) \quad (3)$$

3D source convoluted PSF calculations give equation 4

$$L_{3D} = (s - b)I_{3D} + b \quad (4)$$

where integral I_{3D} is defined as the sum of two error functions according to each direction, shown in equation 5.

$$I_{3D} = \frac{1}{(\sigma_x, \sigma_y, \sigma_z)\sqrt{8\pi^3}} \int_{-\frac{l_x}{2}}^{\frac{l_x}{2}} \int_{-\frac{l_y}{2}}^{\frac{l_y}{2}} \int_{-\frac{l_z}{2}}^{\frac{l_z}{2}} e^{-\frac{(x-x')^2}{\sigma_x^2} - \frac{(y-y')^2}{\sigma_y^2} - \frac{(z-z')^2}{\sigma_z^2}} = \frac{1}{2} \left[\text{erf}\left(\frac{x+\frac{l_x}{2}}{\sigma_x\sqrt{2}}\right) - \text{erf}\left(\frac{x-\frac{l_x}{2}}{\sigma_x\sqrt{2}}\right) \right] \times \frac{1}{2} \left[\text{erf}\left(\frac{y+\frac{l_y}{2}}{\sigma_y\sqrt{2}}\right) - \text{erf}\left(\frac{y-\frac{l_y}{2}}{\sigma_y\sqrt{2}}\right) \right] \times$$

$$\frac{1}{2} \left[\operatorname{erf} \left(\frac{z + \frac{l_z}{2}}{\sigma_z \sqrt{2}} \right) - \operatorname{erf} \left(\frac{z - \frac{l_z}{2}}{\sigma_z \sqrt{2}} \right) \right]$$

$$I_{3D} = I_{1D}(x, l_x, \sigma_x) \times I_{1D}(y, l_y, \sigma_y) \times I_{1D}(z, l_z, \sigma_z) \quad (5)$$

The integral ratio gives in equation 6 an analytic function of measurable parameters that depends on the source dimension and sigma image PSF system.

$$H_{3D}(x, \sigma_x; y, \sigma_y; z, \sigma_z) = \frac{\int_{-\frac{l_x}{2}}^{\frac{l_x}{2}} \int_{-\frac{l_y}{2}}^{\frac{l_y}{2}} \int_{-\frac{l_z}{2}}^{\frac{l_z}{2}} I_{3D}(x, l_x, \sigma_x; y, l_y, \sigma_y; z, l_z, \sigma_z) dx dy dz}{\int_{-\infty}^{+\infty} \int_{-\infty}^{+\infty} \int_{-\infty}^{+\infty} I_{3D}(x, l_x, \sigma_x; y, l_y, \sigma_y; z, l_z, \sigma_z) dx dy dz} \quad (6)$$

The analytic function H_{3D} is used in equation 7 to calculate corrected source count concentration s as a function of b , average value of the counts concentration in the image

background, evaluated away from the source, C_{image} average value of the counts concentration in the image VOI, directly measurable on the image space.

$$s = \frac{1}{H_{1D}(x, \sigma_x) \times H_{1D}(y, \sigma_y) \times H_{1D}(z, \sigma_z)} C_{image} - b \frac{1 - H_{1D}(x, \sigma_x) \times H_{1D}(y, \sigma_y) \times H_{1D}(z, \sigma_z)}{H_{1D}(x, \sigma_x) \times H_{1D}(y, \sigma_y) \times H_{1D}(z, \sigma_z)} \quad (7)$$

(Spill out) (spill in)

s is corrected with both factors: factor which corrects the effect of loss of counts on the image space inside the VOI (spill out) and factor that corrects the effect of increase of counts on the image space inside the VOI due to the background (spill in).

The radius of both the detectors was fixed to 25 cm.

(ii). IEC NEMA Phantom Measurements

The IEC NEMA Body phantom volume and the six spheres were filled with ^{99m}Tc mixed with distilled water using a sphere-to-background (SBR) activity concentration ratio of 10: 1. To obtain the concentration in the spheres and the background with precision, the procedure that follows was established. Firstly, the total activity was measured by an activity calibrator. Secondly, the concentration of the spheres was obtained by mixing the measured activity with 1000 mL of distilled water and the spheres were filled by a precision syringe. Finally, the phantom (background) was filled with the remaining ^{99m}Tc solution by adding distilled water into the phantom, thus obtaining the SBR equal to 10: 1. Special precautions have been taken to ensure a good homogeneity of the radioactive solution. The concentrations are presented in Table 1.

The phantom measurements were performed with activity concentrations of 170.2 and 451.0 KBq/mL. The phantom was positioned in the COR (center of rotation), at the center of the FOV (field of view), as made for the previous acquisition.

2.2.2. Experimental SPECT Acquisitions

This work involved two major experimental steps. The first part about was the sigma measurement of the PSF system using a point source. The second step was to determine the radionuclide count concentration from the image acquisition of the six spheres inserted inside the IEC NEMA phantom.

(i). Point Source Acquisitions

A ^{99m}Tc point source was prepared with an activity of ^{99m}Tc equal to 1.3 mCi introduced into the tip of a small syringe. The PSF of the system was evaluated under different conditions to match the acquisition protocol and parameters used for the phantom experiment. Measurements were made by placing the point source at the center of the field of view (FOV) and in conjunction with the COR (center of rotation).

Table 1. Activity concentration of ^{99m}Tc solution prepared for the two measurements.

Measure 1	The activity of ^{99m}Tc inside the syringe without needle	Quantity of ^{99m}Tc used	Residual activity	The volume of distilled water used (mL)	The concentration of ^{99m}Tc solution prepared
hot sphere	4.67mCi (172790 KBq)	4.60mCi (170200 KBq)	0.068mCi (2516 KBq)	1000	170.2 KBq/mL
background				9800	17.0 KBq/mL
SBR					10: 1

Table 1. Continued.

Measure 2	The activity of ^{99m}Tc inside the syringe without needle	Quantity of ^{99m}Tc used	Residual activity	The volume of distilled water used (mL)	The concentration of ^{99m}Tc solution prepared
hot sphere	12.28 mCi (454360 KBq)	12.19mCi (451030 KBq)	0.0878mCi (3248.6 KBq)	1000	451.0 KBq/mL
background				9800	45.1 KBq/mL
SBR					10: 1

The data reconstruction parameters and filter employed in this work are summarized in Table 2. For Chang's method attenuation correction using CT was employed, and the

reconstructed slices were centred, reoriented and saved using Xeleris software.

Table 2. OSEM reconstruction algorithm parameters.

N°	Reconstruction algorithm	Iteration and subset	filter
1	OSEM	2 iterations, 10 subsets	Butterworth (fc=0.48, p=10) ACSC
2	OSEM	2 iterations, 10 subsets	ACSC

2.2.3. Point Spread Function (PSF) Evaluation

Point source images were used to estimate the system's PSF, which was characterized by standard deviation (σ), assuming a Gaussian profile [6]. The three horizontal (x), vertical (y) and axial (z) profiles were extracted from the central region of the image and a Gaussian fit was made using image J software. The goodness of the fit was assessed by the calculation of correlation coefficient R^2 [12].

2.2.4. Count Recovery

LIFEx v7.3.0 software was used to perform three-dimensional (3D) segmentation of spherical VOIs. Six VOIs of appropriate diameter according to the theoretical sphere size (37 mm, 28 mm, 22 mm, 17 mm, 13 mm, 10 mm) were drawn on the SPECT images of the first dataset (OSEM, 2 iterations, 10 subsets, with and without Butterworth filter, ACSC) as accurately possible in correspondence with the hot spheres. Four VOIs were also drawn in correspondence of the background (bkg) to evaluate counts concentration. Background 3D ROIs had a specific volume and were placed on areas and slices of the phantom sufficiently far from the hot spheres, in locations identified as Up Left, Up Right, Bottom Left and Bottom Right. The total counts from the

spheres in the background were averaged. Total counts from all the six hot spheres 3D ROIs and from the four background 3D ROIs were recorded for each composite image, thus for all the reconstructed datasets for both activities' concentration. Once the system PSF was characterized and the counts of the original image (C_{image}) in the six spheres of the resulting phantom images, the recovery formula (equation (7)) was applied to obtain the resulting counts (C_{recover}) and to evaluate the accuracy of the PVE correction method under the different conditions taken into consideration. Recovery after application of the PVE correction, estimated as a percentage difference between C_{image} and C_{recover} , was computed.

3. Results

Measurements were made on both types of experimental situation, point source and IEC NEMA phantom with two different activity concentrations. The following results show the achievement of the system's PSF sigma, count concentration ratio and count concentration in terms of recovery, and their rate of difference after and before the application of post-reconstruction algorithm.

3.1. Sigma of PSF System

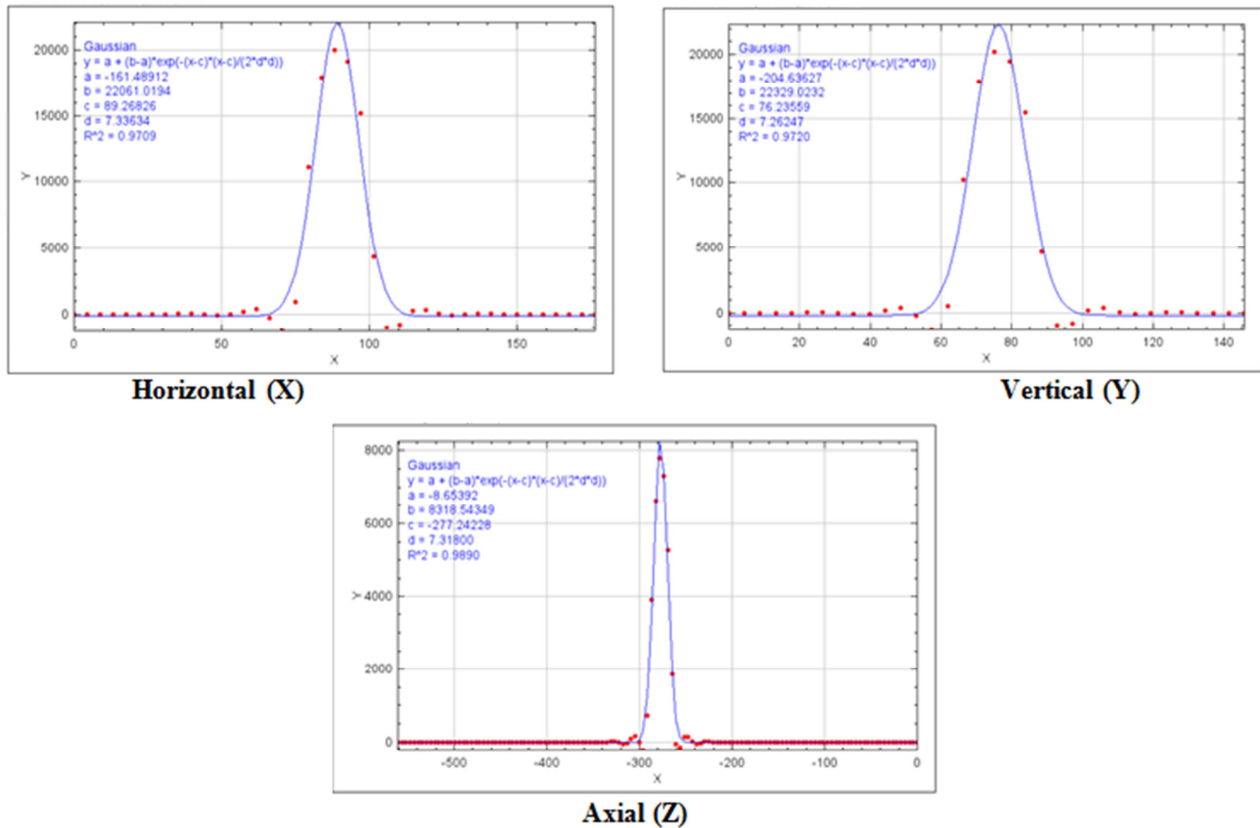
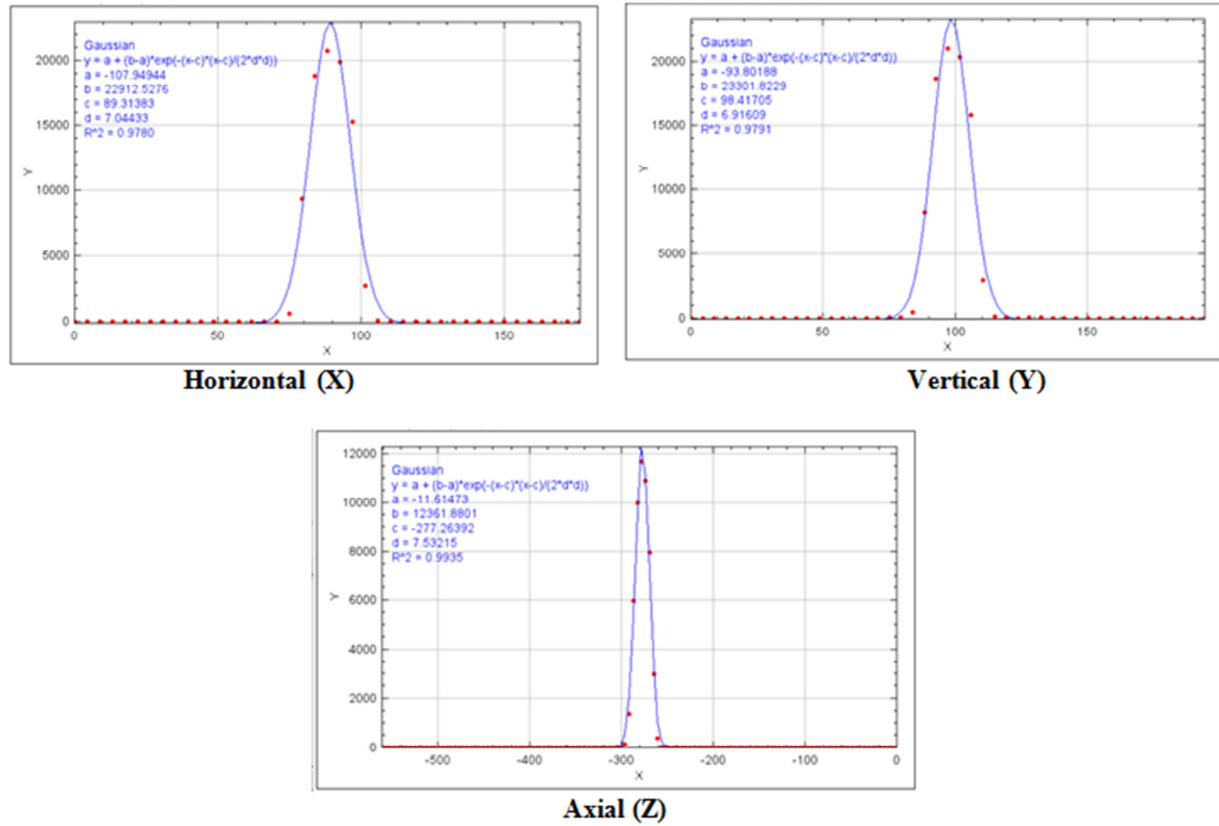
**Figure 1.** Gaussian profile of point source reconstructs by OSEM 2 iterations 10 subsets, ACSC, Butterworth (fc=0.48, p=10).

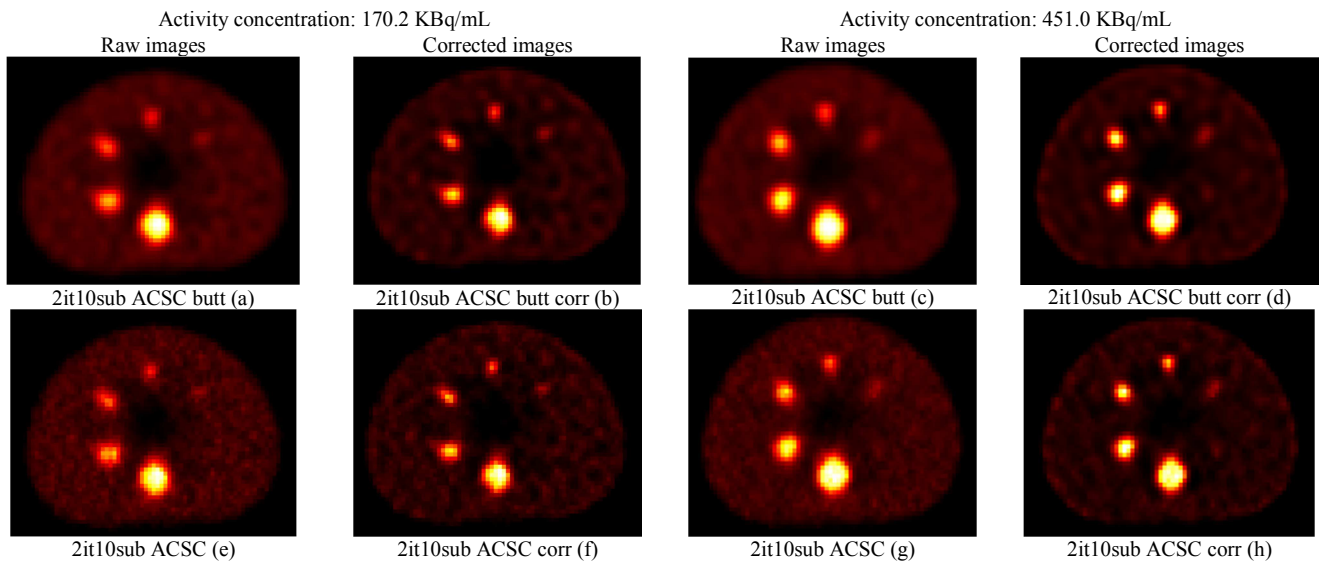
Table 3. Sigma values for both reconstruction OSEM 2 iterations 10 subsets, ACSC with and without Butterworth 0.48.

Reconstruction	σ_x	σ_y	σ_z	σ
OSEM 2 iterations 10 subsets, ACSC Butterworth (fc=0.48, p=10)	7.33	7.26	7.31	12.64
OSEM 2 iterations 10 subsets, ACSC (unfiltered)	7.04	6.91	7.53	12.41

**Figure 2.** Gaussian profile of point source reconstructs by OSEM 2 iteration 10 subsets, ACSC.

3.2. Count Concentration

Count concentration was measured on the hot sphere of the image space. SPECT images of radionuclides in spheres of different diameter sizes are shown respectively in Figure 3.

**Figure 3.** Visualization of the raw and corrected hot sphere images of the IEC NEMA phantom in different experimental situations. OSEM 2 iterations (it) 10 subsets (sub), ACSC reconstructed image. For 170.2 KBq/mL, Butterworth (butt); (a) raw image, (b) corrected (corr) image, unfiltered; (e) raw image, (f) corrected image. For 451.0 KBq/mL, Butterworth; (c) raw image, (d) corrected image, unfiltered; (g) raw image, (h) corrected image.

The corrected source concentration was calculated by Equation 7 for each hot sphere size of the SPECT images obtained in the different experimental situations. The tables below show the result.

Table 4. Image concentration (C_{image}), background concentration (b), corrected source concentration (s) in (counts/mL) at 170.2 KBq/mL.

170.2 KBq/mL	Diameter (mm)	$C_{image} 10^3(\text{counts/mL})$	$b 10^3(\text{counts/mL})$	$s 10^3(\text{counts/mL})$
	OSEM 2 iterations 10 subsets ACSC Butterworth 0.48			
	37	5.43	0.83	8.52
	28	4.06		7.33
	22	3.51		7.56
	17	2.73		7.43
	13	1.81		6.17
	10	1.08		2.75
	OSEM 2 iterations 10 subsets ACSC			
	37	5.40	0.72	8.47
	28	4.07		7.37
	22	3.53		7.65
	17	2.97		8.34
	13	2.00		7.47
	10	1.07		3.88

Table 5. Image concentration (C_{image}), background concentration (b), corrected source concentration (s) in (counts/mL) at 451.0 KBq/mL.

451.0 KBq/mL	Diameter (mm)	$C_{image} 10^3(\text{counts/mL})$	$b 10^3(\text{counts/mL})$	$s 10^3(\text{counts/mL})$
	OSEM 2 iterations 10 subsets ACSC Butterworth 0.48			
	37	13.13	2.41	20.33
	28	9.74		17.18
	22	7.78		15.91
	17	5.56		13.35
	13	3.97		10.92
	10	3.27		8.94
	OSEM 2 iterations 10 subsets ACSC			
	37	13.03	2.38	20
	28	9.70		16.89
	22	7.81		15.75
	17	5.79		13.89
	13	4.14		11.59
	10	3.14		9.18

3.3. Count Concentration Ratio

The corrected count concentration, the raw count concentration and their different percentage rate for each hot

sphere size of the SPECT images obtained in the different experimental situations are presented in the tables and figures below.

Table 6. Count Concentration ratio and sphere dimension (l/σ) estimated for 170.2 KBq/mL.

170.2 KBq/mL									
Sphere diameter	l^a	l/σ	Raw conc ratio ^b	Corr conc ratio ^c	True ratio	Raw ^d (%)	Corr ^e (%)	Corr-Raw ^f (%)	Corr-Raw
With Butterworth	10	0.79	1.30	3.31	10.00	-87.00	-66.9	20.10	0.20
	13	1.03	2.18	7.44		-78.20	-25.6	52.60	0.53
	17	1.34	3.29	8.95		-67.10	-10.5	56.60	0.57
	22	1.74	4.23	9.11		-57.70	-8.9	48.80	0.49
	28	2.21	4.89	8.84		-51.10	-11.6	39.50	0.40
	37	2.93	6.54	10.26		-34.60	2.6	37.20	0.37
Without Butterworth	10	0.81	1.50	5.43	10.00	-85.00	-45.7	39.30	0.39
	13	1.05	2.80	10.44		-72.00	4.4	76.40	0.76
	17	1.37	4.16	11.67		-58.40	16.7	75.10	0.75
	22	1.77	4.94	10.70		-50.60	7	57.60	0.58
	28	2.26	5.69	10.30		-43.10	3	46.10	0.46
	37	2.98	7.56	11.84		-24.40	18.4	42.80	0.43

^asphere diameter

^bRaw conc ratio: raw count concentration ratio, ^cCorr conc ratio: corrected count concentration ratio.

V_{bkg} : background volume

Percentage difference in counts measured on raw and corrected images:

Percentage of counts relative to true ratio:

$$\text{conc ratio} = \frac{\text{count of VOI}/\text{VOI}}{\text{count bkg}/V_{\text{bkg}}} \quad (8)$$

$$^f \text{Corr} - \text{Raw}(\%) = \text{Corr}(\%) - \text{Raw}(\%) \quad (9)$$

$$^d \text{Raw}(\%) = 100 \times (\text{Raw conc ratio} - \text{true})/\text{True} \quad (10)$$

$$^e \text{Corr}(\%) = 100 \times (\text{Corr conc ratio} - \text{true})/\text{True} \quad (11)$$

From Tables 6 and 7, the curves of the raw or corrected concentration ratio with respect to the sphere dimension were plotted and illustrated in Figure 4.

Table 7. Count Concentration ratio and sphere dimension (l/σ) estimated for 451.0 KBq/mL.

451.0 KBq/mL									
Sphere diameter	l	l/σ	Raw conc ratio	Corr conc ratio	True ratio	Raw (%)	Corr (%)	Corr-Raw (%)	Corr-Raw
With Butterworth	10	0.79	1.36	3.72	10.00	-86.40	-62.8	23.60	0.24
	13	1.03	1.65	4.54		-83.50	-54.6	28.90	0.29
	17	1.34	2.31	5.55		-76.90	-44.5	32.40	0.32
	22	1.74	3.23	6.61		-67.70	-33.9	33.80	0.34
	28	2.21	4.05	7.14		-59.50	-28.6	30.90	0.31
	37	2.93	5.45	8.45		-45.50	-15.5	30.00	0.30
Without Butterworth	10	0.81	1.32	3.85	10.00	-86.80	-61.5	25.30	0.25
	13	1.05	1.74	4.87		-82.60	-51.3	31.30	0.31
	17	1.37	2.43	5.83		-75.70	-41.7	34.00	0.34
	22	1.77	3.28	6.61		-67.20	-33.9	33.30	0.33
	28	2.26	4.07	7.09		-59.30	-29.1	30.20	0.30
	37	2.98	5.47	8.39		-45.30	-16.1	29.20	0.29

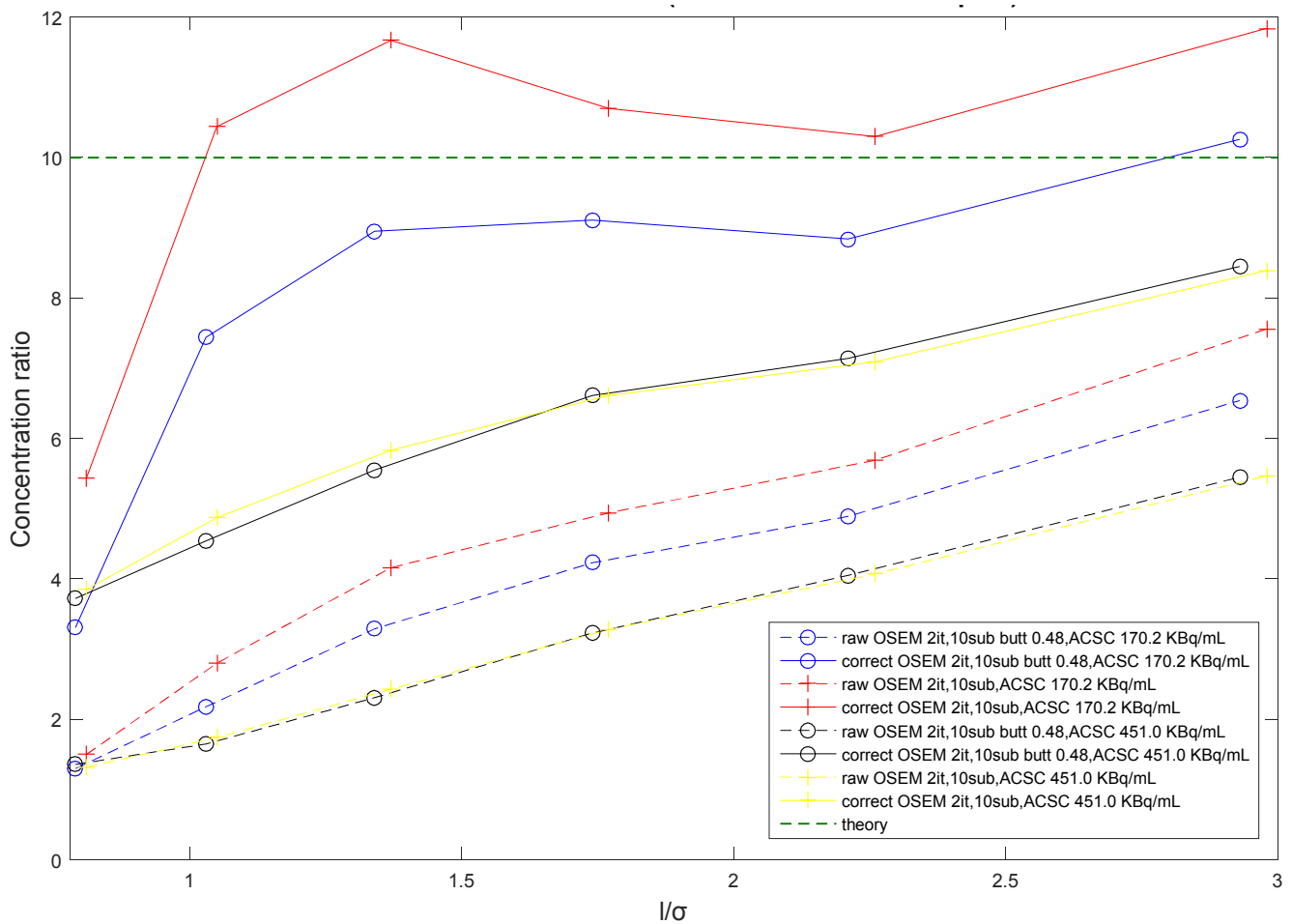


Figure 4. Concentration ratio vs l/σ (170.2 and 451.0 KBq/mL).

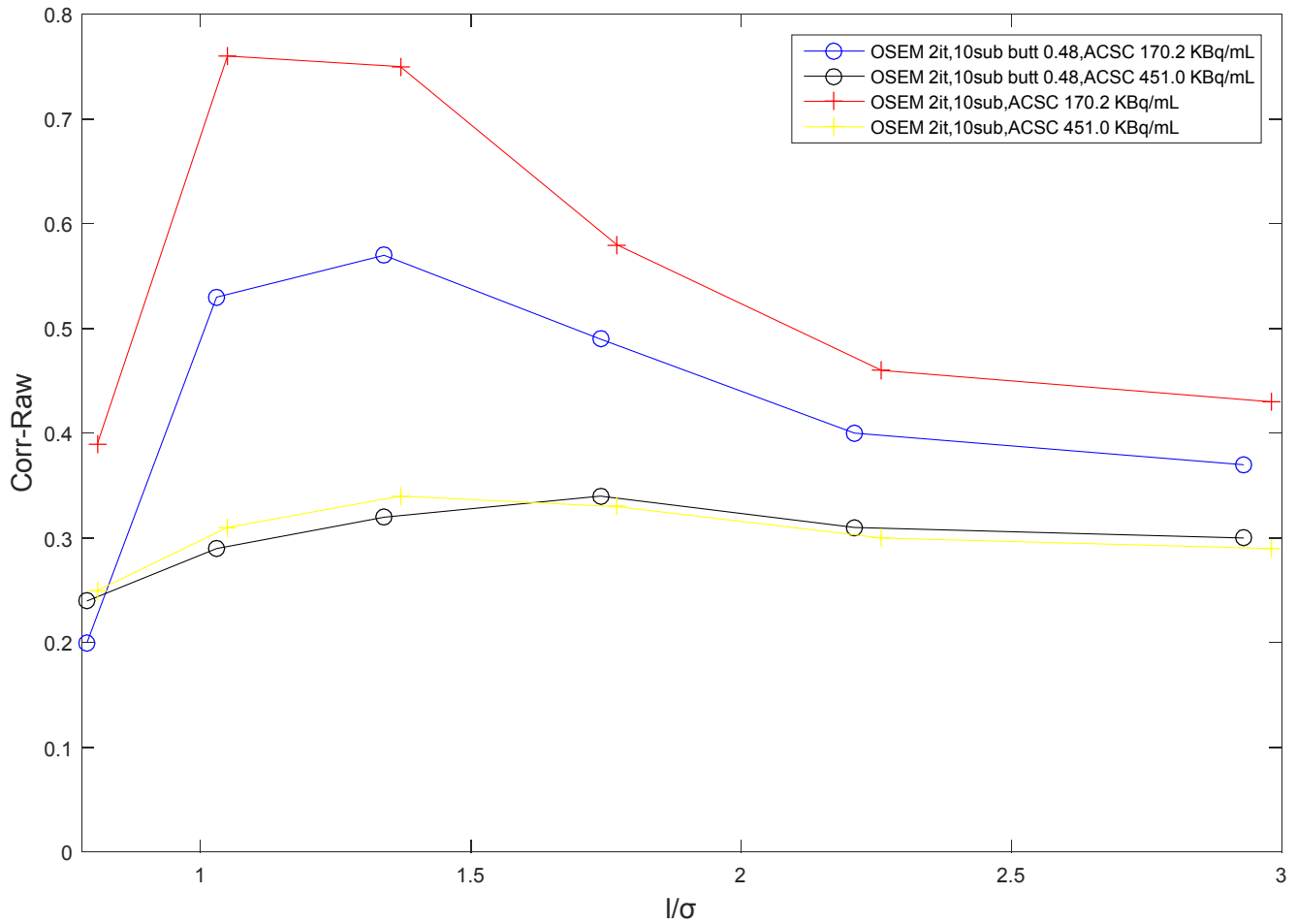


Figure 5. Difference corr-raw vs l/σ , (170.2 and 451.0 KBq/mL).

The raw concentration ratio is represented by the solid line curves and the corrected concentration ratio is represented by the dashed curves (Figure 4). The improvement between the raw and corrected concentration rate is shown in Figure 5.

4. Discussion

The purpose of this work was to implement a post-reconstruction algorithm to correct PVE in SPECT imaging in order to improve image quality and quantification. This method has already been approved for PET imaging [5] and now, gives in its first application on SPECT imaging the acceptable results. In general, post-processing corrective methods offer multiple advantages over those built into the reconstruction algorithm [13]. The dimensions of the spheres inserted in phantom being known, the spatial resolution of the system was determined in terms of sigma through a point source using the clinical protocol TARE. Indeed, sigma and sphere size were used to configure the analytical function H_{3D} (see equation 6) in the post-reconstruction algorithm. The sigma value of the PSF system is available in Table 3. The data from the point source acquisition were adjusted by Gaussian curves giving the correlation coefficient R^2 in the range from 0.97 to 0.99. This indicator is shown to have good statistical significance. The resulting Gaussian equation gives us the sigma value by the parameter d shown in Figures 1 and 2. The sigma module has almost the

same value for both reconstructions, namely 12.64 and 12.41 respectively. This is probably due to the noises present in the images that were not perfectly managed during the reconstruction process. In the figure 3, the SPECT images obtained showed good visualization of radionuclides of different diameters as well as regions of high and low radionuclide concentration of the corrected images. The source corrected concentration (Tables 4 and 5) was obtained from Equation 7 to improve the count of losses due to the spill phenomenon (spill-out and spill-in) during reconstruction. H_{3D} corrects this defect in both spills. A concentration ratio of 10 was used. From the concentration of each volume of interest, a ratio to the background concentration was calculated for the reconstructed and post reconstructed image in order to evaluate the recovery and compare it to the experimental value. Tables 6 and 7 present the count concentration ratio and sphere dimension (diameter per sigma) for the concentration activities of filtered and unfiltered images. The difference between Raw (%) and Corr (%) percentages was calculated to show the percent estimate value relative to the true concentration, (i. e., 10) equation 9. Negative values represent under-estimated concentration ratios and positive values represent overestimated ratios. The difference between these two estimates shows the effect of the rate of increase due to the PVE correction in different situations. These values showed that the algorithm improves image quality accurately.

Figure 4 shows the comparison of the concentration ratio (y-axis) before and after the application of the PVE recovery method to different experimental situations. In Figure 4, at 170.2 KBq/mL, only the ratio of the Butterworth corrected image for the largest sphere (blue curve) and the unfiltered corrected image for all other spheres, except the smallest (red curve), achieved a ratio greater than 10. Figure 5 shows that the correction rate is high for the low activity concentration. The difference between corrected and raw is more obvious for the smaller spheres, except for the first one (red and blue curves). The mean difference when we consider the three peak points in Figure 5 of the sphere size of the 13 mm, 17 mm and 22 mm, gives the percentage improvement rate of PVE correction for images with Butterworth is approximately 52.66% at 170.2 KBq/mL versus 31.7% at 451.0 KBq/mL respectively and for images unfiltered is about 70 % at 170.2 KBq/mL versus 32.87% at 451.0 KBq/mL respectively (figures 5 and 6). A recent study reveals that when the filter has been applied to reconstructed images, the post-filter increases the degree of negative bias in smaller objects, but removes the positive bias, due to noise, present in larger spheres of unfiltered images [14]. For 28 mm and 37 mm spheres in Figure 5, the percentage improvement rate of PVE correction for images with Butterworth is approximately 38.35% at 170.2 KBq/mL versus 30.45% at 451.0 KBq/mL respectively and for images unfiltered is around 44.45% at 170.2 KBq/mL

versus 29.7% at 451.0 KBq/mL respectively. Also, for the smallest 10mm sphere in Figure 5, the percentage improvement rate of PVE correction for images with Butterworth filter is approximately 20.1% to 170.2 KBq/mL versus 23.6% to 451.0 KBq/mL respectively and for images unfiltered is around 39.3% at 170.2 KBq/mL versus 25.3% at 451.0 KBq/mL respectively. The results show that it is difficult to recover the count for small spheres and this is generalized on all spheres when it is a concentration of activity too high as was the case in this study (i.e., 451.0 KBq/mL). The histogram in Figure 6 illustrates this. Previous work on SPECT quantification shows that the use of an activity concentration below 300 KBq/mL gives relatively acceptable results in which the use of optimal planar imaging parameters reduces the impact of PVE, this improves quantitative accuracy [15]. The correction rate is more accurate with the low activity concentration than for the high activity concentration which means that the PVE is more present when we use high activity. The same observation was done in the work of Mohd Fahmi et al, where the recovery coefficient decreases when the activity is high [16]. The best recovery of account losses is demonstrated in this study with the measurement performed with the activity concentration of 170.2 KBq/mL, image reconstructed by OSEM 2 iterations, 10 subsets, ACSC of photons, unfiltered whose post reconstruction shows a percentage improvement rate compared to the raw image of about 70%.

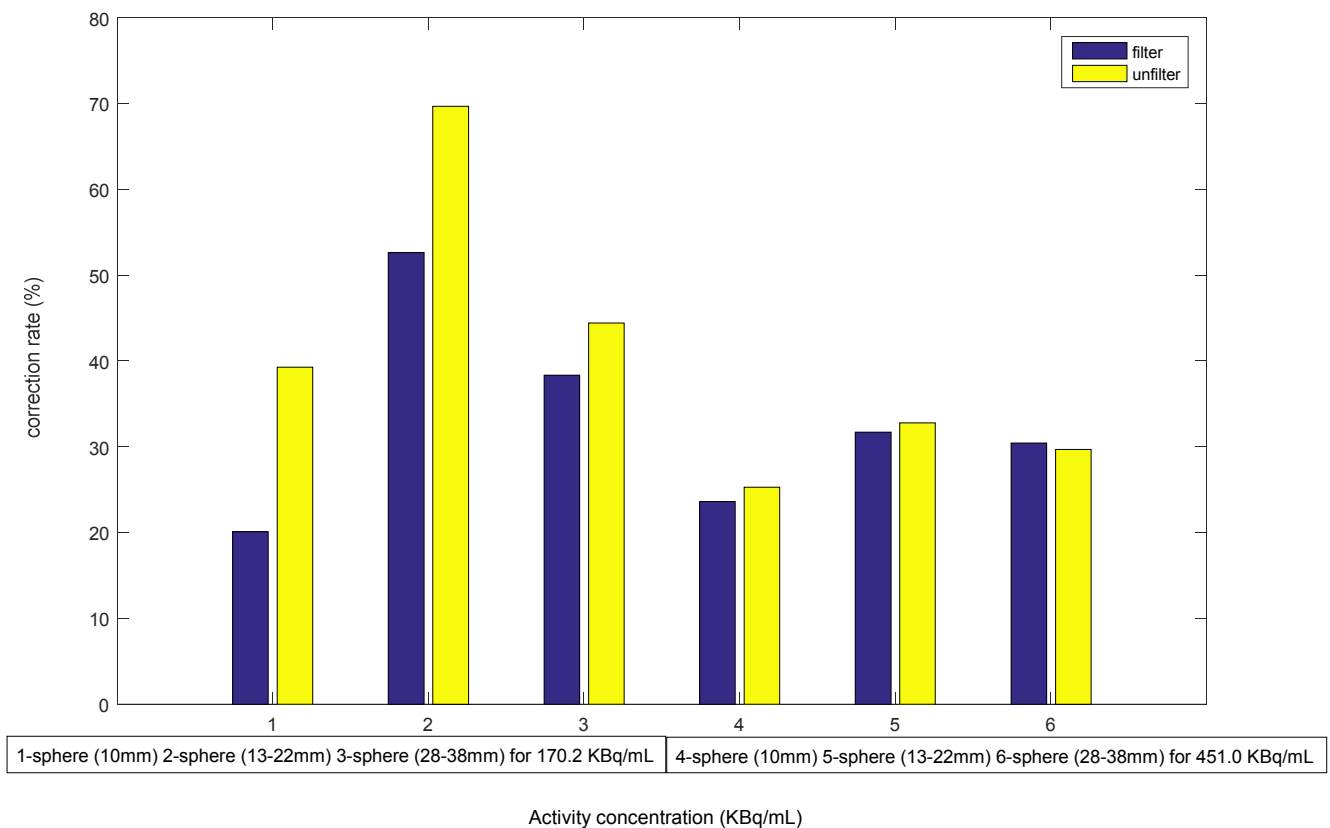


Figure 6. Percentage of PVE correction rate between raw and corrected images.

5. Conclusion

The post reconstruction method for PVE correction applied on SPECT images was found to be effective for IEC NEMA phantom measurements. Although this work has shown a correction rate of up to 70% for medium-sized spheres (13 to 22 mm) as shown in Figures 4 and 5, it can be further improved and extended to other spheres in different experimental situations. This algorithm is based on the mathematical theory of convolution and depends on the PSF of the system and the dimension of the object to be studied for its configuration. It is a powerful and easy to use tool. Therefore, the main limitations of phantom assessments were: sphere filling; segmentation procedure; PSF measurement. This method is an alternative post-treatment method to the recovery coefficient method. In perspective, since the PVE correction is performed by the analytical function H_{3D} which is an error function, it can therefore be improved by using the complementary error function or another distribution like Poisson. This could be a lead investigator in our future work. This method can also be tested on other machines in other nuclear medicine departments to improve quantification procedures for clinical purposes.

Conflict of Interest

No conflict of interest.

Acknowledgements

The study was performed by Medical Physics research team in Côte d'Ivoire, ICTP, Trieste University and Pisa University Hospital in Italy.

The authors acknowledge with gratitude the support from the team.

References

- [1] Kojima A, Matsumoto M, Takahashi M, Hirota Y, Yashida H. Effect of spatial resolution on SPECT quantification values. *J Nucl Med* 1989; 30 (4): 508–14.
- [2] Clarke LP, Leong LL, Serafini AN, Tyson IB, Silbiger ML. Quantitative SPECT imaging: influence of object size. *Nucl Med Commun* 1986; 7 (5): 363–72.
- [3] Jaszczak JR, Coleman RE, Wittehead FR. Physical factors affecting quantitative measurement using camera based single photon emission computed tomography (SPECT). *IEEE Trans Nucl Sci* 1981; 28: 69–80.
- [4] IAEA Human Health Reports No. 9 2014 Quantitative Nuclear Medicine Imaging Concepts, Requirements and Methods (Vienna: International Atomic Energy Agency).
- [5] Di Martino, F.; Barca, P.; Bortoli, E.; Giuliano, A.; Volterrani, D. Correction for the Partial Volume Effects (PVE) in Nuclear Medicine Imaging: A Post-Reconstruction Analytic Method. *Appl. Sci.* 2021, 11, 6460. <https://doi.org/10.3390/app11146460>
- [6] Marine Soret, Stephen L. Bacharach, and Irene Buvat. Partial-Volume Effect in PET Tumor Imaging. *J Nucl Med* 2007; 48: 932–945. DOI: 10.2967/jnumed.106.035774.
- [7] Andreas Grings, Camille Jobic, Torsten Kuwert and Philipp Ritt. The magnitude of the partial volume effect in SPECT imaging of the kidneys: a phantom study. Grings et al. *EJNMMI Physics* (2022) 9: 18 <https://doi.org/10.1186/s40658-022-00446-2>
- [8] Frouin V, Comtat C, Reilhac A, Gregoire MC. Correction of partial-volume effect for PET striatal imaging: fast implementation and study of robustness. *J Nucl Med.* 2002; 43: 1715–1726.
- [9] Mpumelelo Nyathi, Enoch Sithole2, Ouma Ramafi, Quantification of partial volume effects in planar imaging. *Iran J Nucl Med* 2016; 24 (2): 115-120.
- [10] Marquis H, Willowson KP, Bailey DL. Partial volume effect in SPECT & PET imaging and impact on radionuclide dosimetry estimates. *Asia Ocean J Nucl Med Biol.* 2023; 11 (1): 44-54. doi: 10.22038/AOJNMB.2022.63827.1448.
- [11] C Nioche, F Orlhac, S Boughdad, S Reuzé, J Goya-Outi, C Robert, C Pellot-Barakat, M Soussan, F Frouin, and I Buvat. LIFEx: a freeware for radiomic feature calculation in multimodality imaging to accelerate advances in the characterization of tumor heterogeneity. *Cancer Research* 2018; 78 (16): 4786-4789. www.lifexsoft.org
- [12] ImageJ software, 1.54f; Java 1.8.0_265 [64-bit]. [Internet]. 2023 [cited 2023 August 04]. Available from: <http://imagej.net/software/Fiji/download.html>
- [13] Gong, K.; Cherry, S. R.; Qi, J. On the assessment of spatial resolution of PET systems with iterative image reconstruction. *Phys. Med. Biol.* 2016, 61, N193–N202.
- [14] John C. Dickson, Ian S. Armstrong, Pablo Minguez Gabiña, Ana M. Denis-Bacelar, Aron K. Krizsan, Jonathan M. Gear, Tim Van den Wyngaert, Lioe-Fee de Geus-Oei, Ken Herrmann. EANM practice guideline for quantitative SPECT-CT. *Eur J Nucl Med Mol Imaging* (2023) 50: 980–995. <https://doi.org/10.1007/s00259-022-06028-9>.
- [15] Mpumelelo N. Determination of Optimum Planar Imaging Parameters for Small Structures with Diameters Less Than the Resolution of the Gamma Camera. *Iran J Med Phys* 2017; 14: 219-228. 10.22038/ijmp.2017.24559.1246.
- [16] Mohd Fahmi Mohd Yusof, Umami Solehah Ab Ghani, Nor Amalyna Ghazali, Ahmad Thaifur Khaizul, Abdullah Waidi Idris. Evaluation of contrast and recovery coefficients as performance parameters in planar and SPECT imaging. 2020 IOP Conf. Ser.: Mater. Sci. Eng. 785 012046.